University Library



A gateway to Melbourne's research publications

Minerva Access is the Institutional Repository of The University of Melbourne

Author/s:
McCoey, JM;de Gille, RW;Nasr, B;Tetienne, J-P;Hall, LT;Simpson, DA;Hollenberg, LCL

Title:
Rapid, High-Resolution Magnetic Microscopy of Single Magnetic Microbeads

Date:
2019-05-01

Citation:
McCoey, J. M., de Gille, R. W., Nasr, B., Tetienne, J. -P., Hall, L. T., Simpson, D. A. & Hollenberg, L. C. L. (2019). Rapid, High-Resolution Magnetic Microscopy of Single Magnetic Microbeads. Small, 15 (18), https://doi.org/10.1002/smll.201805159.

Persistent Link:
https://hdl.handle.net/11343/270998

Rapid, High-resolution Magnetic Microscopy of Single Magnetic Microbeads

Julia M. McCoey, Robert W. de Gille, Babak Nasr, Jean-Philippe Tetienne, Liam T. Hall, David A. Simpson,[*] Lloyd C. L. Hollenberg

J. M. McCoey, R. W. de Gille, Dr. JP. Tetienne, Dr. L. T. Hall, Dr. D. A. Simpson, Prof L. C. L. Hollenberg, School of Physics, University of Melbourne, Parkville, 3010, Australia

Dr B. Nasr
Centre for Neural Engineering, University of Melbourne, Melbourne, 3053, Australia
The Department of Electrical and Electronic Engineering, The University of Melbourne, VIC, 3010, Australia.

Keywords: magnetic beads, magnetic imaging, diamond, ferromagnetism, superparamagnetism

ABSTRACT

Magnetic microparticles or 'beads' are used in a variety of research applications from cell sorting through to optical force traction microscopy. The magnetic properties of such particles can be tailored for specific applications with the uniformity of individual beads critical to their function. However, the majority of magnetic characterization techniques quantify the magnetic properties from large bead ensembles. Developing new magnetic imaging techniques to evaluate and visualize the magnetic fields from single beads will allow detailed insight into the magnetic uniformity, anisotropy and alignment of magnetic domains. Here, diamond-based magnetic microscopy is applied to image and characterize individual magnetic beads with varying magnetic and structural properties: ferromagnetic and superparamagnetic/paramagnetic, shell (coated with magnetic material) and solid (magnetic material dispersed in matrix). The single-bead magnetic images identify irregularities in the magnetic profiles from individual bead populations. Magnetic simulations account for the varying magnetic profiles and allow us to infer the magnetization of

individual beads. Additionally, this work shows that the imaging technique can be adapted to achieve illumination-free tracking of magnetic beads, opening the possibility of high resolution tracking cell movements and mechanics studies in photosensitive contexts.

1. Introduction

Magnetic beads are in use in biomedical and environmental sciences for a wide range of applications including enzyme immunoassays[1], magnetic cell separation [2], [3], detection of environmental trace elements [4], hyperthermia [5], [6], and targeted drug delivery [7]. The different applications of magnetic beads necessitate different physical properties (i.e. size, shape and magnetic properties) and novel applications are continually being explored. In the quest for optimized magnetic beads, properties such as individual uniformity, homogeneity throughout the sample[8], and magnetic properties including the saturation magnetization, coercivity, and magnetic susceptibility play a critical role. Improving these characteristics requires reliable, reproducible methods to examine them.

The size and shape of magnetic beads can be characterized well with existing methods such as dynamic light scattering (DLS) or electron microscopy techniques [9]–[12]. Techniques that can characterize the magnetic properties, on the other hand, are limited. High temperature scanning (HTS) superconducting quantum interference device (SQUID) measurements can image magnetic features but have a limited spatial resolution in the tens of microns[13], which is greater than the largest typical magnetic microbeads. Magnetic beads can be imaged by magnetic resonance imaging (MRI), and are in fact used as MRI contrast agents [14], however the spatial resolution of MRI (typically on the order of mm, but reaching tens of μm[15]) means it cannot determine the properties of individual beads. Magnetic force microscopy can produce images of magnetic fields, but interpretation is not straight forward, as the magnetic tip can interact with the sample under

investigation. The scanning probe geometry of this technique also makes assessment of multiple beads time-consuming. Magnetotransport techniques using hall[16] and domain wall sensors[17] have demonstrated single magnetic bead detection, however these single point sensors are limited in throughput and often require precise placement to measure the magnetic signals from an individual magnetic bead. Other optical-based techniques such as magneto-optical indicator film (MOIF)[18], [19] or magneto-optical Kerr effect (MOKE)[20], [21] have provided detailed magnetic information on the spin hall effect and magnetic skyrmions with high spatial resolution. However, imaging the superparamagnetic properties of materials at the sub-micron scale in a biologically relevant environment remains a significant challenge for all the aforementioned techniques.

To overcome these limitations, we have applied quantum magnetic microscopy (QMM) [22], [23] to image individual magnetic beads of various designs: beads evenly dispersed with superparamagnetic material ('solid') (see Figure 1a), beads coated with superparamagnetic material ('shell') (see Figure 1b) and ferromagnetic beads (see Figure 1c). QMM relies on the nitrogen vacancy (NV) center in diamond[24] to image local micron scale magnetic fields. NV-based imaging has previously been demonstrated on a variety of magnetic materials and systems, including bacteria[25], magnetic recording material[17], FeNiCr nanoparticles[26], cell lines labelled with magnetic particles[27], and micromagnets[28] (30 μm to 110 μm rectangular nickel/iron prisms). Here, we apply QMM to investigate the magnetic properties of individual micron-sized magnetic beads at room temperature with diffraction-limited spatial resolution (~440 nm)[17] and a wide field of view, sufficient to image multiple beads in a sample at once.

The microscope setup used is illustrated in figure 1d and described previously[17]. An NV imaging layer was engineered within approximately 10 nm of the diamond surface of a [111] crystal, affixed atop a lithographically patterned gold microwave waveguide on a glass coverslip.

The NV center consists of a nitrogen atom and vacancy at adjacent sites of the diamond cubic lattice. The negatively charged NV center is a spin 1 system with a paramagnetic ground state triplet. In the presence of a magnetic field, the paramagnetic ground states Zeeman split the m_s = -1 and m_s = +1 spin states with a gyromagnetic ratio of 2.8 MHz/G. The NVs can be optically initialized into the m_s = 0 state with 532 nm laser excitation. The microwave frequency required to drive the NV center to the m_s = -1 and m_s = +1 states is related to the magnetic field via the gyromagnetic ratio. Transition to the m_s = ±1 states is detected via a reduction in fluorescence intensity, as the decay pathway of the NV when excited from the m_s = ±1 states includes the possibility of a non-radiative route, resulting in a ~10% reduction in fluorescence when compared with decay of the NV excited from the m_s = 0 spin state. This optically detected magnetic resonance (ODMR)[29], [30] forms the basis of static magnetic field imaging for the super/paramagnetic and ferromagnetic beads. The magnetic field sensitivity of this method is given by:

$$\eta = \frac{4h\delta}{3\sqrt{3}\cdot g_{NV}\gamma_e R\sqrt{n}}$$

where δ is the full width half maximum of the ODMR peak, and R is the contrast. n is the number of photons/second per detection volume. In the current configuration the measured sensitivity of QMM is 1.5 μT/√Hz.

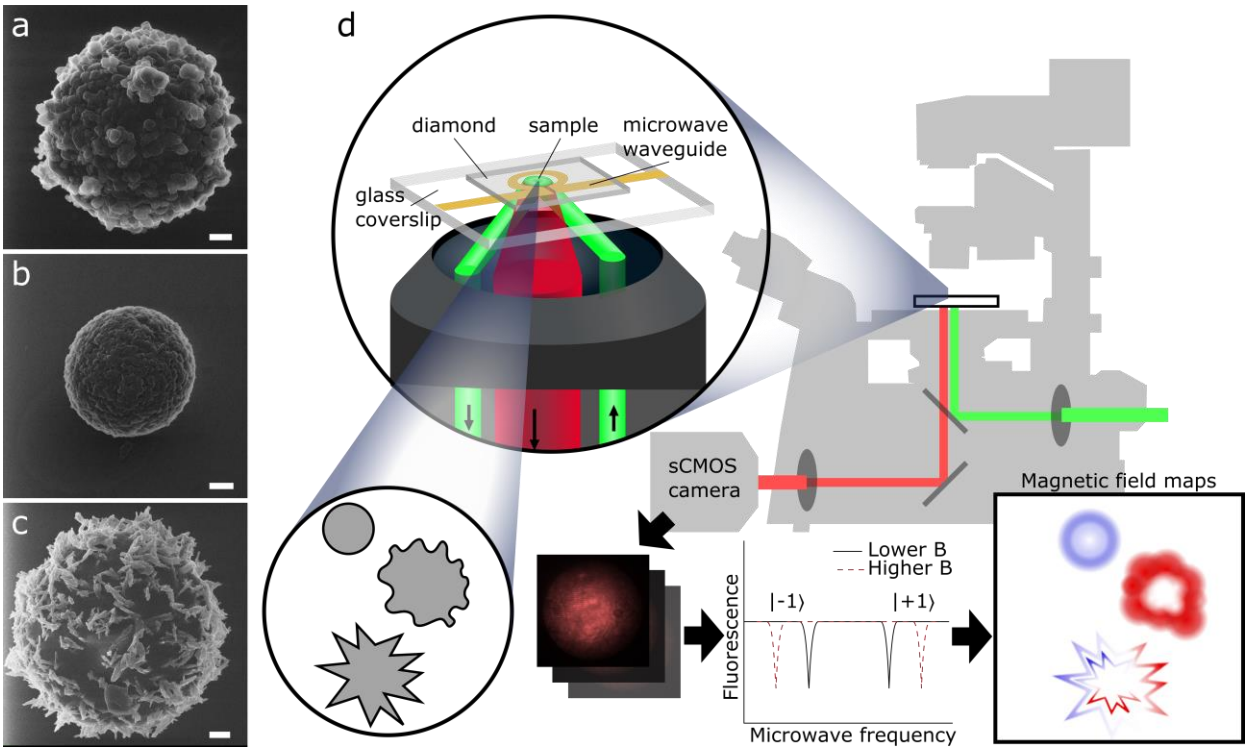


Figure 1. Helium-ion micrographs of (a) polystyrene microsphere coated with magnetite (Spherotech, AMS-40-10H). Scale bar: 500 nm (b) polystyrene microsphere evenly dispersed with maghemite (gamma-Fe_2O_3) and magnetite (Fe_3O_4) (Dynabeads M-270). Scale bar: 500 nm (c) polystyrene microsphere coated with chromium dioxide (Spherotech, CFM-40-10). Scale bar: 500 nm (d) Schematic representation of workflow. The sample is deposited on a diamond sensor chip containing a layer of nitrogen vacancy centers (NVs). The NV centers are optically excited by a green (532 nm) laser focused onto the sensor through the microscope objective; microwave excitation to control the NV spin is delivered via a gold resonator situated below the diamond imaging chip. The NV fluorescence (637-800 nm) is filtered and imaged on a scientific complementary metal–oxide–semiconductor (sCMOS) camera. Fluorescence images are collected and analyzed at various microwave frequencies to construct magnetic field maps.

2. Results and Discussion

2.1. Examining superparamagnetic bead design

We begin by examining superparamagnetic beads typically used in magnetic cell separation and enzyme immunoassays. Beads composed of many superparamagnetic nanoparticles are useful because they behave as a paramagnet, having no remanent magnetic moment when an applied field is removed. Because of this, such beads are usually simply termed paramagnetic beads. Samples of commercially-available beads were loaded on the diamond sensor chip by depositing a 2 μL suspension of beads directly on the diamond surface and allowing the solvent to evaporate. A weak background field (5 mT) was applied perpendicular to the diamond surface to isolate a class of NV centers aligned with the background field, and to induce a net magnetic moment in the beads. The ODMR peaks corresponding to the aligned NVs measure the z-projection of the magnetic field along the NV axis, in this case normal to the diamond surface, see supplementary information. The resulting magnetic profiles are shown in Figure 2.

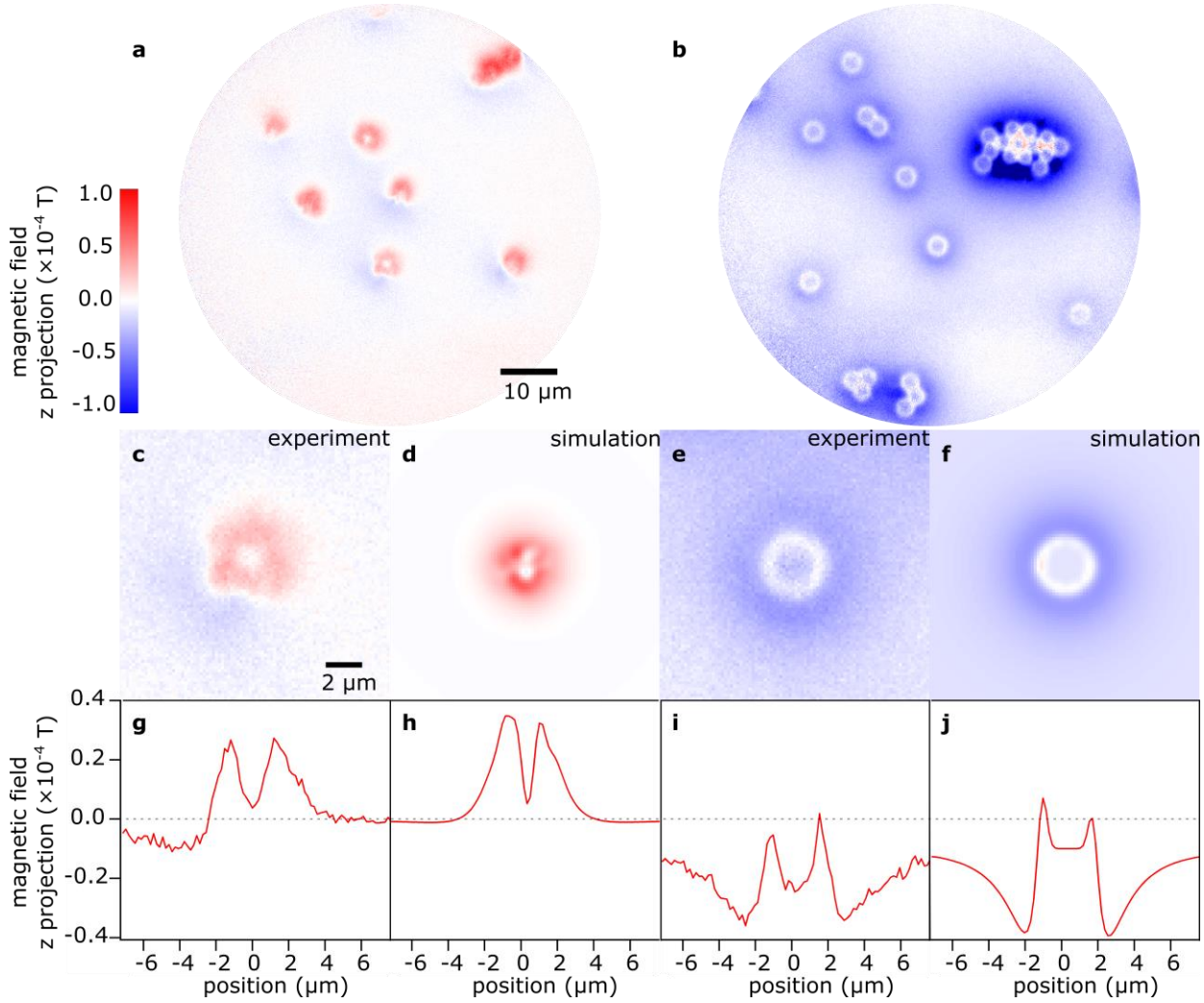


Figure 2. QMM imaging of multiple (a) superparamagnetic shell, and (b) superparamagnetic solid beads. An individual (c) superparamagnetic shell bead produces a magnetic signature in approximate agreement with (d) simulation. (e) An individual superparamagnetic solid bead shows distinct magnetic signature, also in agreement with (f) simulation. Applied background field strength (5 mT towards the +z direction) is subtracted from the field strength values. (g - j) show corresponding line cuts horizontally though the beads corresponding to experiment and simulation for each case. The truncation which is observed below the centre of the beads is due to the dynamic range of the NV sensors as discussed in[26]. The dynamic range and instrument response have been accounted for in the magnetic simulations.

Superparamagnetic shell (nominal diameter 4 μm, Figure 2 a) and superparamagnetic solid beads (nominal diameter 2.8 μm, Figure 2 b) each show a distinct magnetic profile imaged in the xy plane. Both bead types comprise polystyrene spheres with magnetic nanoparticles – the superparamagnetic shell beads are coated in magnetite nanoparticles, and the superparamagnetic solid beads are evenly dispersed with maghemite and magnetite throughout. The superparamagnetic solid beads have an additional thin polystyrene coating while the ferromagnetic and superparamagnetic shell beads have no additional coating beyond the magnetic nanoparticles. The superparamagnetic shell beads (Figure 2 a) display irregular spatial magnetic profiles when compared to the solid beads (Figure 2 b), which exhibit more uniform magnetic profiles, indicating a uniform magnetic composition. Close-up views of individual beads are shown in Figure 2c and 2e for the shell and solid type, respectively, with line cuts plotted in Figure 2g and 2i. To validate and understand the shape of the magnetic profiles, both beads' magnetic profiles were simulated with a magnetic model in MATLAB (see supporting information). The models consist of cubic magnetic domains aligned in the z direction, randomly arranged in either a spherical shell or dispersion through a solid sphere. Magnetization and total volume of magnetic material were tuned as free parameters as there were multiple unknown parameters including the density of magnetic nanoparticles, nanoparticle size, and the ratio of maghemite to magnetite. The magnetic modelling (Figure 2 d, f, h, j) is in agreement with the measured profiles. As discerned from the modelling, the central dips in the magnetic field profiles are due to a combination of the geometry of the spheres and a truncation artefact which significantly reduces the measured field when outside the dynamic range of the NV sensors[26]. Modelling shown in the supplementary information indicates that the field projection of the solid beads would be in the positive direction below the center of

the bead, as is the case for the shell beads, in the absence of a truncation artefact. The difference between the magnetic profiles of the shell and solid bead architectures is explained in part by the bead geometry and in part by the overall density of magnetic material – increasing the density of magnetic material scales the intensity of the magnetic profile (Figure S1), and solid bead geometry produces a smoother magnetic profile as compared to the shell geometry (Figure S2). By comparing between models and experimental results, bead diameters can be determined. This was confirmed for the magnetic image shown in Figure 2e. Our modelling predicted a bead diameter of approximately 1.8 μm, significantly less than the 2.8 μm ± 0.2 μm diameter nominated by the supplier; this was subsequently confirmed by helium ion microscopy that showed the bead diameter was 1.83 μm (Figure S3). In addition, from the magnetic images, the magnetization of each bead (averaged over the volume of the sphere) can be estimated, here $M \approx 2\times10^3$ A/m, for this applied field of 5 mT (SI Fig S4). This is in good agreement with measurement of magnetically induced bead velocity[31], when the smaller bead size is considered. Similarly, the magnetization may be estimated for the shell beads (averaged over shell volume); for a shell thickness of 400 nm, $M \approx 2.5\times10^2$ A/m. Comparing the two bead designs, in both the measurements and simulation, interspersing magnetic material through a solid sphere appears more favorable to achieve greater uniformity of magnetic field profile and magnetic field strength. Together these results demonstrate how QMM can be used to validate magnetic bead designs, characterize individual bead magnetic uniformity, potentially providing a new tool for magnetic quality control in the bead manufacturing process.

2.2 Ferromagnetic particle magnetization

Cell mechanics assays use ferromagnetic beads to impart forces and monitor reactions. To image the magnetic signatures of ferromagnetic beads, chromium dioxide-coated beads (nominal diameter 4 μm) were deposited on the diamond and imaged with QMM (Figure 3 a, b). The size and magnetic anisotropy of the chromium dioxide nanoparticles coating the beads is sufficient to retain their magnetization in the absence of an applied field. Unlike the paramagnetic beads, ferromagnetic beads do not produce uniform magnetic profiles, because the magnetic domains of chromium dioxide nanoparticles on the surface of the spheres are randomly aligned, resulting in random magnetic field projections with an overall reduced net magnetic field, significantly less than that produced by the aligned superparamagnetic nanoparticles seen in Figure 2.

In practice, ferromagnetic beads are used in high applied magnetic field applications[32], [33]; these fields align the magnetic domains of the ferromagnetic coated nanoparticles. Figures 3 c and d show how the magnetic dipoles can be manipulated under a strong applied magnetic field in the z-direction, perpendicular to the diamond surface. The ferromagnetic bead profiles change from being randomly oriented to aligned in the direction of the applied field. The magnetic field strength is greatly enhanced following the high field magnetization (> 0.2 T); Figure 3c and d compare the magnetic profiles on the same scale before and after the magnetization, noting both images were obtained under the weak background field of 5 mT. Supplementary video 1 shows the dynamic change in the magnetic order of a single particle with an increasing applied magnetic field.

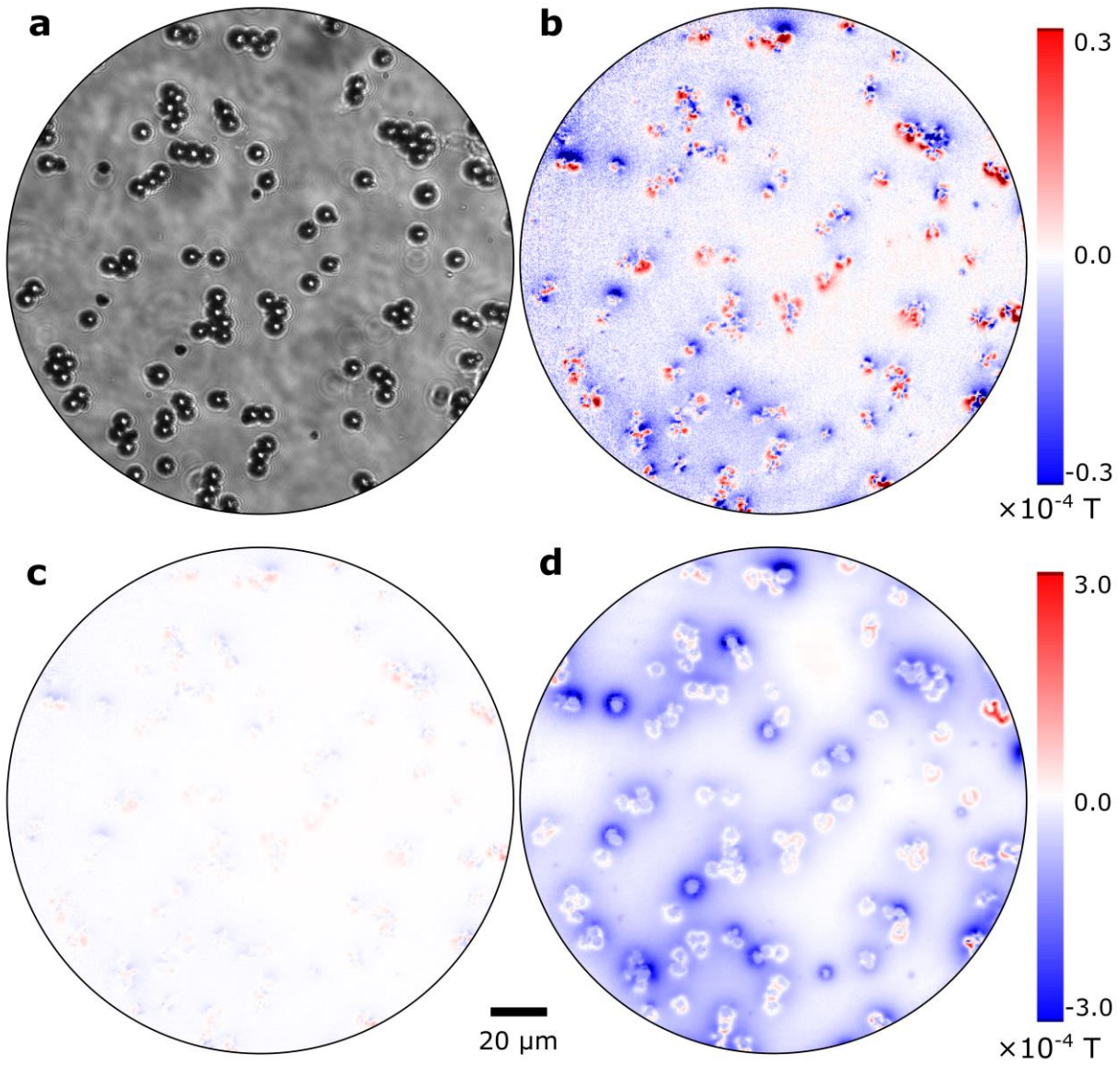


Figure 3. Magnetic alignment of ferromagnetic beads. (a) Bright-field image of chromium dioxide-coated 4 µm beads. (b) Magnetic field map of field strength in z axis, prior to application of strong (> 0.2 T) field. (c) As in (b), but on same magnetic scale as (d). (d) Magnetic field map after application of a strong field > 0.2 T in the z-direction, returned to a weak (5 mT) field. The 5 mT background field has been subtracted in (b-d).

After alignment, the imaging shows varying circular magnetic signatures; some are distinctly more intense than the others. The less intense (0.1-0.2 mT) signatures correspond to regular spheres in the bright-field image (Figure 3 a). The more intense (-0.3 mT) signatures do not correlate with regular spheres in the bright field, but instead with particulate material, smaller and less regular than the spheres. These magnetic signatures were replicated by modelling the system as a combination of spherical shell and solid sphere of aggregated magnetic nanoparticles (Figure 4). The opposite sign resulting from the different geometries of magnetic material is also replicated by our model. This is due to the truncation effect which suppresses the centre of the aggregated magnetic material profile, leaving the outer ring visible in our magnetic images. This image is consistent with the solid small bead which was supported by He-ion imaging of the sample (figure 4 d). It appears that excess chromium dioxide nanoparticles detached from, or not adhered to, the polystyrene microspheres create a buildup of loose, dense, ferromagnetic material in the sample. QMM facilitated the rapid identification of the magnetic contaminant. Additionally, the He-ion microscopy reveals that whilst the polystyrene spheres are highly uniform, the magnetic coating coverage is somewhat irregular, explaining the remaining irregularity in their magnetic signature even after magnetization. These results highlight that the uniformity of the polystyrene microsphere substrate does not guarantee the magnetic uniformity of the beads after coating.

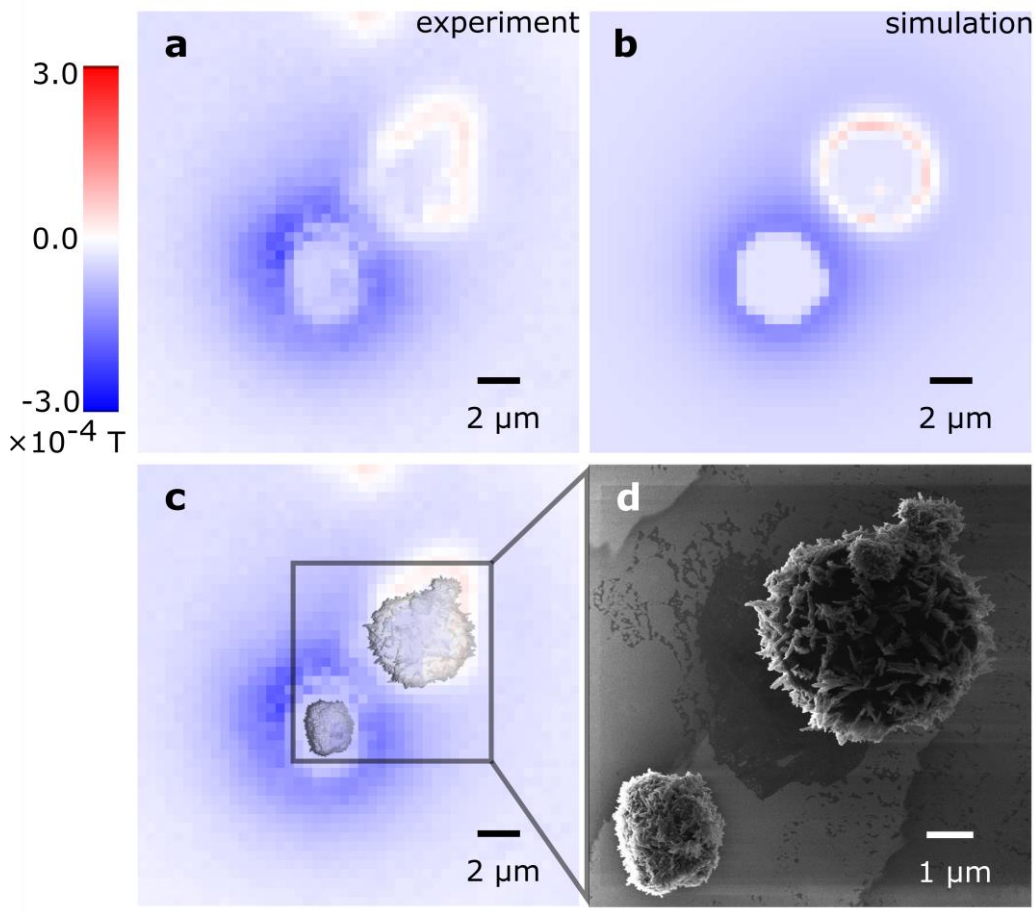


Figure 4. Simulation of spherical shell and solid ferromagnetic particles. (a) Measured magnetic field map of ferromagnetic particles after application of strong field. (b) Simulation of magnetic field from solid and spherical shells; see SI Figure S4. (c) Location of particles imaged by helium-ion microscopy, shown in inset, (d).

2.3 Superparamagnetic signal detection

Magnetic beads can exhibit paramagnetic behavior even though the magnetic material is magnetite and/or maghemite, minerals that are generally ferrimagnetic. At room temperature, small (less than about 10 nm) magnetite nanoparticles are superparamagnetic, but synthesis methods can influence the magnetic properties of the nanoparticles (reviewed in [34]). Under an applied magnetic field, the superparamagnets exhibit a non-zero net magnetic moment imaged

above. Similar to a paramagnet, the magnetization disappears upon removal of the applied field, making the beads invisible to standard magnetic imaging techniques. However, the superparamagnetic state also gives rise to fast magnetic fluctuations which can be imaged by a derivative of QMM, quantum relaxation microscopy (QRM)[35]–[37].

QRM images are generated by mapping the spin lattice relaxation time of the NV sensing probes. The NV spin relaxation time is measured by optically polarising the spin state using 532 nm light. The NV spin can then evolve in the dark and interact with the magnetic environment both inside and outside the diamond. This interaction causes the NV spin to relax to a thermal equilibrium of the three triplet ground spin states. The longitudinal relaxation rate, $1/T_1$, will be affected by environmental magnetic field fluctuations at frequencies at the NV Larmor precession frequency, $\omega_0 = D \pm \gamma B_0$, where γ is the gyromagnetic ratio, B_0 is the applied magnetic field and D is the NV zero-field splitting. A fluctuating magnetic field, such as that provided by a superparamagnetic nanoparticle, will result in a decrease in the NV T_1 time (an increase in the T_1 rate) provided the fluctuation frequency of the superparamagnet is in the order of the $|0\rangle$ to $|\pm1\rangle$ transition frequency of the NV, which is ~3 GHz at zero magnetic field. Mapping the T_1 rate across the diamond sensor will therefore map areas of GHz fluctuating fields. Given that the T_1 rates remain within the dynamic range (kHz-GHz) of the NV sensors, no truncation effect is observed in QRM. High QRM signals can affect QMM, as fast T_1 relaxation rates can reduce the spin polarisation efficiency and overall ODMR contrast, however the QRM signals observed in this work are orders of magnitude away from this regime.

To assess the superparamagnetic nature of the magnetic beads, QRM images of both the superparamagnetic shell (Figure 5a) and solid (Figure 5b) beads were acquired. QRM can be performed consecutively with QMM with no differing sample preparation requirements. Figure 5

presents QRM images from a region of interest shown in Figure 2, allowing for direct comparison between QMM and QRM. Magnetic signals are observed in both QMM and QRM; this indicates the presence of paramagnetic and superparamagnetic behaviour in a single magnetic bead. This is not surprising, as the size distribution of iron oxide nanoparticles is not uniform as seen in the high resolution He-ion electron microscopy images (Figure 1). Both samples produced similar magnetic relaxation profiles, despite their different magnetic geometry. This is attributed to the sensing height of NV imaging array in this imaging modality (limited to ~100 nm[37]) and fluctuating magnetic signal fall off ($1/r^3$). Even so, this imaging mode is particularly useful for probing the magnetic fluctuation spectrum for novel superparamagnetic materials.

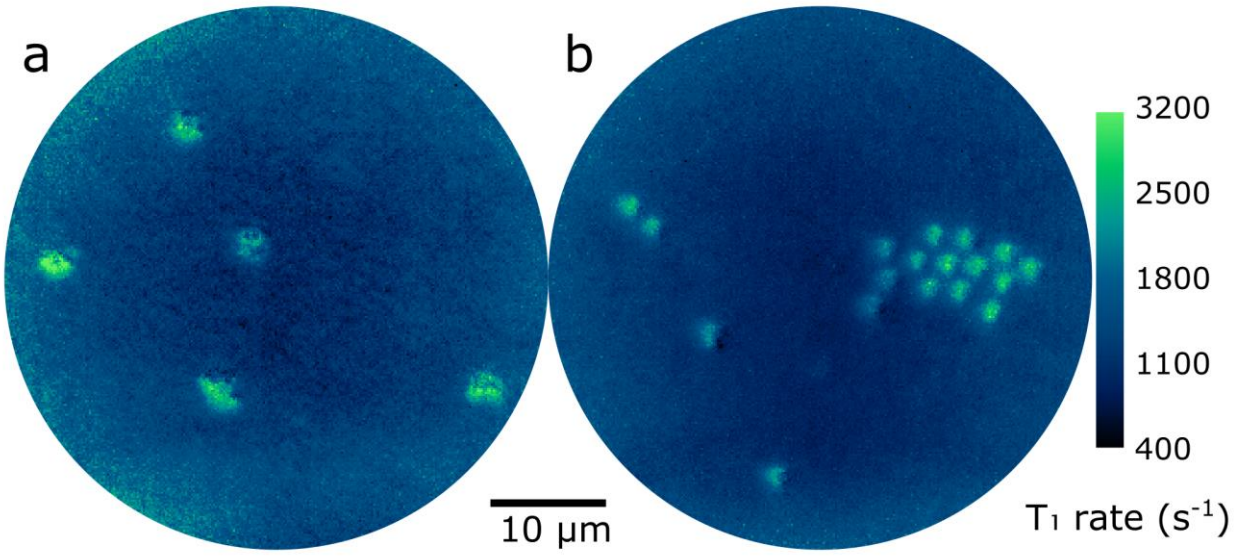


Figure 5. Quantum relaxation images of superparamagnetic beads. Magnetic fluctuation signal from (a) solid superparamagnetic beads (Dynabeads M-270) and (b) shell superparamagnetic beads (Spherotech AMS-40-10H), imaged via the NV T_1 rate.

2.4 Rapid illumination-free bead localization

Many of the biological applications of magnetic beads include functionalization of the particle. For instance, beads may be functionalized with antibodies to target and label certain populations of cells, for sorting. For tracking, however, fluorescent tags are ubiquitous in the biosciences. Fluorescent tags have facilitated a large portion of what is now known of cell behaviors and movements in live cell imaging, whether they be targeted to cell membranes, or embedded in a substrate on which cells are cultured, as in traction force microscopy (TFM). However, phototoxicity is a significant challenge for live cell studies [38], [39].The damaging effects of light are particularly of concern in time lapse imaging where long exposure to irradiation causes cell death. More insidious are the cases when cell death is not detected, but effects of the illumination are nevertheless occurring, thus confounding conclusions drawn from data. In addition to cell damage, photodamage is experienced by some photosensitive drugs, causing difficulty in assessment of their effects on cell behavior.

Magnetic bead imaging and tracking may provide an alternative approach to optical tagging for mechanical cytometry[40] and traction[41] studies. To determine whether QMM can be applied to image and track the location of magnetic beads, we modified the microscope for total internal fluorescence microscopy. In this imaging mode, the excitation light is confined to the diamond with the evanescent tail of the excitation penetrating only a few hundred nm's above the diamond surface. This ensures that magnetic imaging and tracking of individual beads can be performed with extremely weak optical fields interacting with the sample. Imaging movement of a tag requires image acquisition times short enough for the speed of the movement to be recorded; for example, small cell lung cancer cells move at a speed of 16 μm/hour and *Bdellovibrio bacteriovorus* hunts its bacteria prey at speeds of 160 μm/second [42].

To investigate the temporal resolution of QMM for single magnetic bead tracking, we applied a modified ODMR imaging protocol to probe a single microwave frequency to maximize sensitivity to small magnetic field changes. This allows fast qualitative detection of changes in magnetic field via a change in the fluorescence intensity of the NV centers, which is sufficient for locating and tracking magnetic particle positions and trajectories.

To determine the cumulative image acquisition time required to reliably pinpoint the location of magnetic beads, we acquired single-frequency ODMR images over increasing intervals (Figure 6). The signal-to-noise ratio of the magnetic profiles (Figure 6 a) increases with acquisition time as expected. To systematically detect magnetic beads, we used a Hough transform to detect circles in 100 replicate experiments of each acquisition time (Figure 6 b). 60% of magnetic beads were detected within 600 ms, and 95% were detected within five seconds. The standard deviation in the coordinates of the center of the fitted circle is less than 200 nm after 800 ms image acquisition and less than 125 nm after 5 s. This imaging time is more than sufficient for long term cell tracking applications and TFM. In an application setting, beads may be present in solution or dispersed in substrate hundreds of nanometers above the sensor surface. To gain an indication of the performance of ferromagnetic beads under these conditions, we simulated the magnetic profile at increasing heights above the sensor (see supporting information). This preliminary analysis indicates solid beads would be more suitable than shell, as with increasing stand-off, they retain a stronger signal with a smaller bead size (Figure S5).

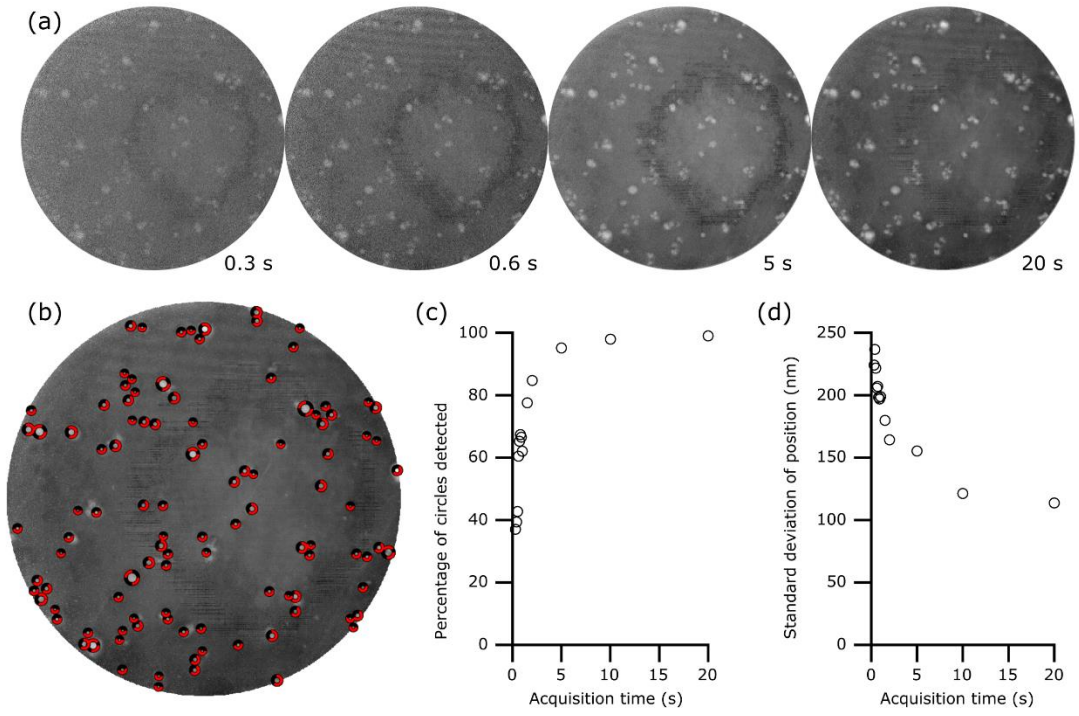


Figure 6: Single magnetic bead tracking via QMM. Superparamagnetic beads are imaged with single frequency ODMR. (a) Series of single frequency ODMR of beads at increasing acquisition times. (b) Algorithm for single particle identification using a Hough transform in MATLAB; circles indicate the detected beads within the field of view. (c) Percentage of circles detected by Hough transform after total acquisition time of averaged images. (d) Standard deviation of the circle center as detected with Hough transform after total acquisition time of averaged images.

3. Conclusion

This work demonstrates that QMM is a powerful analysis and screening technique for imaging the magnetic properties of individual magnetic beads. We show QMM has several key capabilities useful in the development of novel beads, broadly in two categories: (i) High spatial resolution:

Magnetic maps probe individual beads' magnetic structure, providing more detailed information than bulk methods, allowing design on the level of single bead architecture. Whilst high-power imaging techniques can show the morphology of individual beads, physical morphology is not necessarily correlated with the magnetic structure - polystyrene spheres coated in magnetic material may be highly uniform in size, but this does not guarantee magnetic uniformity. (ii) High throughput: The field of view and reasonably rapid image acquisition allows assessment of bead homogeneity, rapid identification of magnetic contaminants in a sample, which may be undetectable via other techniques such as SQUIDs; additionally, as NV sensing is compatible with microfluidics[43], the technique could be extended to more rapidly characterize multiple bead sample preparations in succession.

As well as a useful tool in analysis of magnetic beads during their development, we show QMM has the potential to create new cytological assays altogether, as an illumination-free tagging and tracking technique. False positives were minimal, and would not be expected to pose a challenge to modern tracking algorithms (for a recent analysis, see [44]). Furthermore, given ferromagnetic beads can be imaged with or without a background magnetic field, we can manipulate the beads in solution or a biological environment to impart mechanical stress, as in twisting cytometry [40], [45]. The movement could then be visualized using QMM and mechanical parameters such as cell stiffness could then be extracted. Additionally, the high magnetic sensitivity of QMM provides scope to image and track magnetic particles less than 100 nm in size for small biological targets.

We believe the techniques presented here could become standard methods in the suite of characterization of novel engineered magnetic beads from a few hundred nanometers to several microns in size. The high throughput nature of the imaging technique can provide rapid profiling

of magnetic properties and opens up a new magnetic imaging capability at the sub-micron scale in biological environments.

4. Experimental section

4.1 Materials

Electronic grade Type IIa <111> diamond (Element 6) were thinned, cut and re-polished to a 1 × 2 × 0.1 mm^3 crystal. NV defects were engineered via ion implantation of ^{15}N atoms at an energy of 4 keV and dose of 1×10^{13} ions/cm^2, followed by annealing at 1000 °C for three hours and acid-treatment (sulfuric acid (1 ml) and sodium nitrate (1 g) at 500°C for 10 min) to remove any surface contamination. NV depth range was between 5-10 nm as indicated by molecular dynamic simulations[46]. Post annealing, the density of NV centers was 1×10^{11} NV/cm^2.

4.2 Sample preparation for imaging

Magnetic beads (Spherotech CFM-40-10 and AMS-40-10H, Dynabeads M-270)) were diluted 1 in 100 v/v in de-ionized water, and deposited in a small (~1μL) drop on the diamond, and allowed to evaporate in the absence of an applied background field.

4.3 NV Imaging

Imaging was performed on a modified Nikon inverted microscope (Ti-U). Samples were pipetted onto the implanted face of the diamond and dried. Background magnetic fields from a neodymium permanent magnet were applied perpendicular to the diamond surface along a <111> crystallographic axis. NV fluorescence was imaged in wide-field with optical excitation from a 532 nm Verdi laser focused (f = 300 mm) onto an acousto-optic modulator (Crystal Technologies Model 3520–220) and then expanded and collimated (Thorlabs beam expander GBE05-A) to a beam diameter of 10 mm. The collimated beam was focused using a wide-field lens (f = 300 mm) to the back aperture of the Nikon x60 (1.4 NA) oil immersion objective via a Semrock dichroic

mirror (Di02-R561-25 × 36). The beam was first centered to the objective for EPI fluorescence imaging and then translated to perform total internal reflection microscopy. The NV fluorescence was filtered using two bandpass filters (650-750 nm) before being imaged using a tube lens (f = 300 mm) onto a sCMOS camera (Neo, Andor). Microwave excitation to drive the NV centers was applied via a 1μm thick omega-shaped gold antenna (diameter=0.8mm) lithographically patterned onto a glass coverslip, upon which the diamond was mounted. The microwave signal (0 dBm) from an Agilent microwave generator (N5182A) was switched using a Miniciruits RF switch (ZASWA-2-50DR+). The microwave signals were amplified by a 40 dBm microwave amplifier (Giga-Tronics GT-1000A) delivering 10W power to the microwave antenna. The broadband antenna provided uniform power across the field of view that was imaged. A Spincore Pulseblaster (ESR-PRO 500 MHz) was used to control the timing sequences of the excitation laser, microwaves and sCMOS camera and the images where obtained and analyzed using custom LabVIEW code. The excitation power density used for imaging was 30 W/mm^2 and all images were taken in an ambient environment at room temperature.

4.4 Helium ion microscopy

Images of the surfaces of microspheres were obtained via a helium ion microscope (HIM), (Carl Zeiss, Orion Nanofab, Peabody MA, USA). An Everhart-Thornley (E-T) detector was used to image the samples as only secondary electrons were studied in the HIM. The HIM imaging was performed at an optimal accelerating voltage of 30 kV, an aperture size of 10 mm and a reduced helium ion beam current of 0.3 pA while any accumulated charges on glass substrates was easily suppressed by an equipped electron beam flood gun.

The HIM is armed with a very low voltage electron gun (flood gun) to compensate positive surface charge accumulation on the insulating component of the magnetic microbeads. Under these

experimental conditions, no obvious beam damage or change in morphology was observed on the surface of magnetic beads. During imaging the electron beam energy and the X and Y deflectors were adjusted correspondingly to ensure that the best possible image can be obtained.

4.5 Image analysis

Custom LabVIEW code was written for the image analysis of ODMR spectra. The magnetic field images were obtained by binning the camera images 2x2, resulting in a spatial dependence of 85, 142, or 222 nm per pixel for ×100, ×60, and ×40 Nikon objectives respectively. ODMR spectra corresponding to the aligned NV axis were obtained for each binned pixel of the image stack. The magnetic images were displayed and manipulated with ImageJ (Fiji distribution, ImageJ 1.51h). Single-frequency ODMR images were analyzed with MATLAB code. Circles were detected using the Hough transform [47] in sets of 100 replicates of each acquisition time, and the standard deviation of the position of the circle centers of those circles detected in at least 50 of the replicates was found.

Supporting Information

Supporting Information is available from the Wiley Online Library or from the author.

Acknowledgements

This work was supported by the Australian Research Council (ARC) through Grants No. FL130100119, LP130100857 and DE170100129. J.-P.T. acknowledges support from the University of Melbourne through an Early Career Researcher Grant. This work was performed in part at the Materials Characterization and Fabrication Platform (MCFP) at the University of Melbourne and the Victorian Node of the Australian National Fabrication Facility (ANFF).

Received: ((will be filled in by the editorial staff))

Revised: ((will be filled in by the editorial staff))

Published online: ((will be filled in by the editorial staff))

Corresponding author: *E-mail: simd@unimelb.edu.au

[1] L. Reverté, D. Garibo, C. Flores, J. Diogène, J. Caixach, and M. Campàs, *Environ. Sci. Technol.*, **2013**, *47*, 1.

[2] S. Miltenyi, W. Müller, W. Weichel, and A. Radbruch, *Cytometry*, **1990**, *11*, 2.

[3] R. S. Molday, S. P. S. Yen, and A. Rembaum, *Nature*, **1977**, *268*, 5619.

[4] Y. Zhao *et al.*, *Chem. Eng. J.*, **2014**, *235*.

[5] R. Hergt, S. Dutz, R. Müller, and M. Zeisberger, *J. Phys. Condens. Matter*, **2006**, *18*, 38.

[6] J.-H. Lee *et al.*, *Nat. Nanotechnol.*, **2011**, *6*, 7.

[7] O. Veiseh, J. W. Gunn, and M. Zhang, *Adv. Drug Deliv. Rev.*, **2010**, *62*, 3.

[8] N. Bohmer *et al.*, *ACS Appl. Mater. Interfaces*, **2017**, *9*, 35.

[9] K. Butter, P. H. H. H. H. Bomans, P. M. M. Frederik, G. J. J. Vroege, and A. P. P. Philipse, *Nat. Mater.*, **2003**, *2*, 2.

[10] M. Hamoudeh and H. Fessi, *J. Colloid Interface Sci.*, **2006**, *300*, 2.

[11] C. Bergemann, D. Müller-Schulte, J. Oster, L. à Brassard, and A. . Lübbe, *J. Magn. Magn. Mater.*, **1999**, *194*, 1–3.

[12] D. Xiao, T. Lu, R. Zeng, and Y. Bi, *Microchim. Acta*, **2016**, *183*, 10.

[13] M. I. Faley *et al.*, *Supercond. Sci. Technol.*, **2004**, *17*, 5.

[14] H. Shokrollahi, *Mater. Sci. Eng. C*, **2013**, *33*, 8.

[15] E. Van Reeth, I. W. K. Tham, C. Heng Tan, and C. Loo Poh, *Concepts Magn Reson Part A*, **2012**, *40*.

[16] L. Di Michele, C. Shelly, P. de Marco, P. See, D. Cox, and O. Kazakova, *J. Appl. Phys.*, **2011**, *110*, 6.

[17] D. A. Simpson *et al.*, *Sci Rep*, **2016**, *6*.

[18] R. Schäfer and A. Hubert, *Magnetic Domains*, *40*, 159. 2000.

[19] A. L. Balk, C. Hangarter, S. M. Stavis, and J. Unguris, *Appl. Phys. Lett.*, **2015**, *106*, 11.

[20] Z. Q. Qiu and S. D. Bader, *Rev. Sci. Instrum.*, **2000**, *71*, 3.

[21] W.-K. Tse and A. H. MacDonald, *Phys. Rev. Lett.*, **2010**, *105*, 5.

[22] S. Steinert *et al.*, *Rev. Sci. Instrum.*, **2010**, *81*, 4.

[23] L. Rondin, J.-P.-P. P. Tetienne, T. Hingant, J.-F. F.-F. Roch, P. Maletinsky, and V. Jacques, *Reports Prog. Phys.*, **2013**, *77*, 5.

[24] M. W. Doherty *et al.*, *Phys. Rep.*, **2013**, *528*, 1.

[25] D. Le Sage *et al.*, *Nature*, **2013**, *496*, 7446.

[26] J.-P. Tetienne *et al.*, *Sensors (Basel).*, **2018**, *18*, 4.

[27] D. R. Glenn *et al.*, *Nat. Methods*, **2015**, *12*, May.

[28] L. Toraille *et al.*, *Nano Lett.*, **2018**, *18*, 12.

[29] E. van Oort, P. Stroomer, and M. Glasbeek, *Phys. Rev. B*, **1990**, *42*, 13.

[30] A. Gruber, A. Dräbenstedt, C. Tietz, L. Fleury, J. Wrachtrup, and C. von Borczyskowski, *Science (80-.).*, **1997**, *276*, 5321.

[31] J. Xu, K. Mahajan, W. Xue, J. O. Winter, M. Zborowski, and J. J. Chalmers, *J. Magn. Magn. Mater.*, **2012**, *324*, 24.

[32] B. D. Hoffman, G. Massiera, K. M. Van Citters, and J. C. Crocker, *Proc. Natl. Acad. Sci. U. S. A.*, **2006**, *103*, 27.

[33] B. Fabry, G. N. Maksym, J. P. Butler, M. Glogauer, D. Navajas, and J. J. Fredberg, *Phys. Rev. Lett.*, **2001**, *87*, 14.

[34] A. S. Teja and P.-Y. Koh, *Prog. Cryst. Growth Charact. Mater.*, **2009**, *55*, 1–2.

[35] J. H. Cole and L. C. L. Hollenberg, *Nanotechnology*, **2009**, *20*, 49.

[36] S. Steinert *et al.*, *Nat. Commun.*, **2013**, *4*, 1.

[37] D. A. Simpson *et al.*, *Nat. Commun.*, **2017**, *8*, 1.

[38] *Nature Methods*, *10*, 12, Nature Research, 26-Nov-2013.

[39] J.-Y. Tinevez *et al.*, *Methods Enzymol.*, **2012**, *506*.

[40] Y. Y. Zhang *et al.*, *Nat. Protoc.*, **2017**, *12*, 7.

[41] H. Yoshie *et al.*, *Biophys. J.*, **2018**, *114*, 9.

[42] R. Milo and R. Phillips, *Cell biology by the numbers*. Garland Science, 2015.

[43] C. F. Ziem, S. N. Go?tz, A. Zappe, S. Steinert, and J. Wrachtrup, *Nano Lett.*, **2013**, *13*.

[44] V. Ulman *et al.*, *Nat. Methods*, **2017**, *14*, 12.

[45] N. Wang and D. E. Ingber, *Biochem. Cell Biol.*, **1995**, *73*, 7–8.

[46] O. Lehtinen *et al.*, *Phys. Rev. B*, **2016**, *93*, 3.

[47] P. V. C. Hough, *2nd Int. Conf. High-Energy Accel. Instrum.*, **1959**, *73*.